Author Manuscript

Author Manuscript

Author Manuscript

Author Manuscript

HHS Public Access

Author manuscript

*Ultrasound Med Biol*. Author manuscript; available in PMC 2016 June 01.

Published in final edited form as:

*Ultrasound Med Biol*. 2015 June ; 41(6): 1711–1725. doi:10.1016/j.ultrasmedbio.2014.12.668.

# On the relationship between microbubble fragmentation, deflation, and broadband superharmonic signal production

**Brooks D. Lindsey**, **Juan D. Rojas**, and **Paul A. Dayton**

Joint Department of Biomedical Engineering, University of North Carolina-Chapel Hill and North Carolina State University, Raleigh

## Abstract

Acoustic angiography imaging of microbubble contrast agents utilizes the superharmonic energy produced from excited microbubbles, and enables high-contrast, high-resolution imaging. However, the exact mechanism by which broadband harmonic energy is produced is not fully understood. In order to elucidate the role of microbubble shell fragmentation in superharmonic signal production, simultaneous optical and acoustic measurements were performed on individual microbubbles at transmit frequencies from 1.75 to 3.75 MHz and pressures near the shell fragmentation threshold for microbubbles of varying diameter. High-amplitude, broadband superharmonic signals were produced with shell fragmentation, while weaker signals (approximately 25% of peak amplitude) were observed in the presence of shrinking bubbles. Furthermore, when imaging populations of stationary microbubbles with a dual-frequency ultrasound imaging system, a sharper decline in image intensity with respect to frame number was observed for 1 μm bubbles than for 4 μm bubbles. Finally, in a study of two rodents, increasing frame rate from 4 to 7 Hz resulted in a decrease in mean steady-state image intensity of 27% at 1000 kPa and 29% at 1300 kPa. While the existence of superharmonic signals when bubbles shrink has the potential to prolong the imaging efficacy of microbubbles, parameters such as frame rate and peak pressure must be balanced with expected re-perfusion rate in order to maintain adequate contrast during *in vivo* imaging.

### Keywords

contrast agent; microbubble; harmonic; superharmonic; cavitation; acoustic angiography; dual-frequency

## INTRODUCTION

Vascular remodeling is an important indicator of disease in cancers of the breast (Nakamura et al. 2005), prostate (Brawer et al. 1994), and colon (Takahashi et al. 1995; Duff et al. 2007). Specifically, studies have shown increased microvessel density and tortuosity to be early indicators of malignancy in several cancers (Brawer et al. 1994; Fox et al. 1995; Takahashi et al. 1995; Nakamura et al. 2005; Bullitt et al. 2006; Duff et al. 2007). A

Corresponding Author: Paul A. Dayton, UNC-NCSU Joint Department of Biomedical Engineering, 304 Taylor Hall, CB 7575, 109 Mason Farm Rd., Chapel Hill, NC 27599, Phone: 919-843-9521, padayton@email.unc.edu.

Author Manuscript Author Manuscript Author Manuscript Author Manuscript

microbubble contrast agent-based ultrasound imaging approach termed “acoustic angiography” has been developed which is capable of acquiring high resolution images of vasculature alone (Gessner et al. 2010; Gessner et al. 2012; Gessner et al. 2013). In this technique, a low frequency pulse (~1–5 MHz) is transmitted by a dedicated transmit element, exciting microbubbles within vasculature to oscillate nonlinearly and to produce broadband harmonic echoes. These echoes are received by a separate high frequency (≥ 10 MHz) receiving element on the same transducer (Bouakaz et al. 2003; Kruse and Ferrara 2005; Martin et al. 2014). By mechanically scanning this dual-frequency transducer, it is possible to acquire high resolution images of vasculature (Fig. 1) and differentiate healthy tissue from tumor-bearing tissue based on visualizing angiogenesis (Gessner et al. 2012; Shelton et al. In review). However, the exact mechanism by which broadband harmonic energy is produced is not fully understood. While microbubble shell fragmentation is one possible source of broadband energy, the relationship between microbubble shell fragmentation and superharmonic echoes has not yet been directly assessed.

When microbubbles oscillate nonlinearly in response to an applied ultrasound pulse, signals are produced which have energy at integer multiples of the transmitted frequency. While early work demonstrated the utility of harmonic echoes at either twice the transmitted frequency (Chang et al. 1995; Porter and Xie 1995) or subharmonic echoes at half the transmitted frequency (Shankar et al. 1998; Shi et al. 1999), separation of microbubble and tissue echoes may be improved when receiving superharmonic echoes occurring at frequencies greater than three times the transmitted frequency. At such frequencies, signal content is broadband rather than confined to discrete bands (Kruse and Ferrara 2005). However, the role of shell disruption in producing these broadband signals is not clear.

The shell fragmentation threshold for ultrasound contrast agents has been investigated by several groups in determining the pressure-frequency relationship in bubble fragmentation (Chomas et al. 2001b; Chen et al. 2003; Yeh and Su 2008). In addition, researchers have presented several methods for acoustic detection of bubble fragmentation relying on different physical phenomena including rebound signals arising from shell rupture and reformation (Ammi et al. 2006), post-excitation signals (King et al. 2010), or narrowband or broadband harmonics of uncertain origin (Madanshetty et al. 1991; Everbach et al. 1997; Tung et al. 2010; Vignon et al. 2013). The proximity of a microbubble to a vessel wall has been shown to influence the number of pulses required for fragmentation of a population of microbubbles, with bubbles at or near a wall requiring fewer pulses for fragmentation and exhibiting a reduced resonance frequency (Caskey et al. 2007; Couture et al. 2009; Casey et al. 2013). Interactions between bubbles have resulted in an increase in bubble fragmentation threshold as concentration increases (Chang et al. 2001; Yasui et al. 2009). Radhakrishnan et al. recently examined the relationship between cavitation and loss of echogenicity, reporting loss of echogenicity of more than 80% in B-mode images prior to the detection of narrowband harmonic signals associated with stable or inertial cavitation (Coussios et al. 2007). The authors of this previous study hypothesize that the decrease in B-mode echogenicity is the result of shell rupture. When viewed in the context of this result, it is unclear whether the broadband superharmonic signals used in superharmonic imaging are the result of events associated with shell fragmentation or shell rupture. To our knowledge,

Author Manuscript Author Manuscript Author Manuscript Author Manuscript

the question of whether bubbles must be broken in order to produce broadband superharmonic signals has not been answered.

In previous studies characterizing the various mechanisms of ultrasound-induced cavitation phenomena in lipid-shelled microbubbles, observed phenomena have been described as fragmentation, dissolution without visible fragmentation, or shrinkage to a stable diameter (Chomas et al. 2001a; Chomas et al. 2001b; Chen et al. 2002; Borden et al. 2005; Bouakaz et al. 2005; Cox and Thomas 2010; Guidi et al. 2010; Kwan and Borden 2010; Casey et al. 2013). Physical mechanisms of core gas loss have been classified as rapid fragmentation, active diffusion, and passive diffusion (Chomas et al. 2001a). In previous studies examining the fragmentation of single microbubbles, Dayton et al. reported fragmentation thresholds as function of transmitted frequency, pressure, and microbubble diameter (Chomas et al. 2001b), while Sijl et al. reported that larger bubbles have an acoustic response which is largely independent of shell structure (Sijl et al. 2008). Alternatively, when B-mode imaging is used to acoustically assess fragmentation in populations of microbubbles, Porter et al. reported acoustic detection of three distinct mechanisms (static diffusion, acoustically driven diffusion, and rapid fragmentation) (Porter et al. 2006), while Haworth et al. demonstrated the ability to form images of stable and inertial cavitation (Haworth et al. 2012).

Of particular interest for imaging are non-destructive or partially-destructive mechanisms of microbubble dissolution. Several research groups have previously investigated shrinking of lipid-shelled microbubbles in response to pulsed ultrasound. In combined optical-acoustical experiments examining the response of microbubbles to low-pressure (PNP <65 kPa), 15-cycle bursts between 2 and 4 MHz, Guidi et al reported changes in damping as bubbles shrink (Guidi et al. 2010). Thomas et al. recently categorized the response of single shrinking bubbles to two successive pulses on the basis of spectral content at the transmitted frequency and twice the transmitted frequency (Thomas et al. 2009). Underlying mechanisms of shrinkage rate and loss of core gas have recently been examined by Cox and Thomas in optical studies using three-cycle pulses at 1.1 MHz and 200 kPa peak-to-peak amplitude (Cox and Thomas 2010; Cox and Thomas 2013). These studies found that bubbles near resonance shrink faster than the theoretical diffusion limit. The authors propose this enhanced diffusive loss may be due to either turbulent fluid around the bubble or sub-resolution “nanofragmentation” of the lipid shell. The present study is unique from previous studies in that superharmonic acoustic responses are acquired with simultaneous optical observations. Single-cycle pulses at peak negative pressures relevant to *in vivo* imaging (100–500 kPa) are also used rather than multi-cycle bursts. Use of single-cycle pulses is necessary for high-resolution imaging as in Fig. 1.

In recent work, we have characterized the broadband superharmonic response of lipid-shelled microbubbles to ultrasound, describing the signal-to-noise ratio (SNR), contrast-to-tissue ratio (CTR), and axial resolution with varying acoustic pressure, frequency, microbubble diameter, and microbubble concentration (Lindsey et al. 2014). In this work, maximum CTR was observed for transmit frequencies in the 1.5–3.5 MHz range. Previous studies in the literature indicate that larger bubbles typically have a higher fragmentation threshold, which increases with transmit frequency (Chomas et al. 2001b). Our recent results include diagnostically-useful CTR levels at pressures of approximately 500 kPa at 3.5 MHz

Author Manuscript Author Manuscript Author Manuscript Author Manuscript

for 4 μm-diameter bubbles—a combination of pressure and frequency at which some larger bubbles may not fragment—indicating the need for further investigation into the underlying relationship between microbubble fragmentation and superharmonic generation. In the current article, we use simultaneous optical and acoustic measurements to examine this relationship at frequencies from 1.75 to 3.75 MHz and pressures near the microbubble fragmentation threshold for single lipid-shelled microbubbles having diameters in the range of 1 to 4 μm. These single bubble results are then extended to populations of bubbles in *in vitro* and *in vivo* imaging experiments performed with a dual-frequency imaging system.

The following terminology will be used in this manuscript to describe bubble destruction. Microbubble or shell "rupture" denotes the formation of any discrete discontinuity through which core gas is able to escape. "Fragmentation" indicates complete destruction of the microbubble shell immediately upon application of an acoustic pulse. "Destruction" encompasses both rupture and fragmentation. "Shedding" indicates loss of lipid shell material. A "shrinking" or "deflating" bubble is one which exhibits a decrease in diameter in response to one or more applied acoustic pulses.

## MATERIALS AND METHODS

### Contrast agent preparation

Microbubbles were formed from lipid solutions as previously described (Streeter et al. 2010) using a 9:1 molar ratio of 1,2-distearoyl-sn-glycero-3-phosphocholine (DSPC-Powder, Avanti Polar Lipids, Alabaster, AL) and polyoxyethylene 40-stearate (PEG40S, Sigma, St. Louis, MO) in a 90 mL solution of phosphate-buffered saline (Fisher Scientific, Pittsburg, PA). Using a sonic dismembrator (Model 500, Fisher Scientific, Hampton, NH) for 15 seconds at 70% power in the presence of decafluorobutane (SynQuest Labs, Alachua, FL), microbubbles were generated via acoustic emulsification by mechanical agitation via tip sonication, sorted via centrifugation (Feshitan et al. 2009), and sized via optical scattering (Accusizer 780A, PSS-NICOMP, Port Richey, FL). In order to ensure a range of diameters, two distributions of microbubbles were used, one centered at approximately 4 μm in diameter and a second centered at approximately 1 μm in diameter (Fig. 2).

### Single bubble simultaneous acoustic-optical experiments

The setup for these experiments (Fig. 3) consisted of an inverted microscope (Olympus IX2, Tokyo, Japan) which shared a common focus with transmitting and receiving transducers. A high speed camera (Photron Fastcam APX-RS, San Diego, CA) captured images from the microscope at 125 frames/s and displayed the result on a monitor in real time. First, a focused annular transducer with a center frequency of 2.25 MHz (Olympus Panametrics, Waltham, MA) was used to transmit a single-cycle waveform. This transducer was calibrated in water at frequencies between 1.75 and 3.75 MHz in 0.5 MHz increments and pressures between 300 and 1300 kPa in 100 kPa increments using a needle hydrophone (ONDA HNA-0400, Sunnyvale, CA) on a three-axis micro-positioning stage (Narishige International USA, East Meadow, NY). A separate 10 MHz receiving transducer (V311, Olympus Panametrics, Waltham, MA) was positioned within the opening of the annular transducer with the acoustic foci aligned at 5.08 cm. After calibration, the hydrophone was

Author Manuscript Author Manuscript Author Manuscript Author Manuscript

replaced with a 200 μm-diameter cellulose tube (Spectrum Laboratories, Inc., Rancho Dominguez, CA). The tube was aligned to the dual optical/acoustic focus using the microscope and micro-positioning system.

After alignment, prepared microbubble contrast agents were diluted until only single bubbles were observed in the optical field of view. The optical field of view was approximately 150 μm × 150 μm, smaller than the receive focal beam diameter of 600 μm. Diluted microbubble solutions were injected into the tube using a custom microinjection system consisting of an ultra-fine screw thread which controls the injection of a syringe plunger with high precision. When a single, stationary bubble was visible within the optical field of view, five consecutive 1-cycle pulses were transmitted (PRF= 2 Hz) on the low-frequency transducer at a specified pressure-frequency combination. Lines of radiofrequency acoustic data from the 10 MHz receiving transducer were acquired after each of the five consecutive pulses by triggering the data acquisition system on the pulse generator. These data were amplified (RITEC BR-640A, Warwick, RI) and sampled at 100 MHz via a 14-bit digitizing board (Signatec PDA14, Corona, CA). Optical data acquired by the camera were recorded to a laptop computer (Lenovo, Morrisville, NC).

After each sample, a new bubble was introduced into the acoustic/optical focus, and the experiment was repeated for a total of 5 measurements of single bubble behavior for pressures from 100 to 500 kPa in 100 kPa increments and frequencies from 1.75 to 3.75 MHz in 0.5 MHz increments. Observations were made on 250 individual bubbles, with an effort made to capture bubbles of varying diameters. In order to investigate a bubble's ability to produce superharmonic energy over many pulses as would be required in real-time imaging, additional experiments were performed in which 4 μm bubbles were interrogated with 50 single-cycle pulses at 1.75 MHz at 200 and 300 kPa (n=2 bubble trials each case. At each frequency-pressure combination, control data with only water in the tube were acquired. Acquired acoustic data were normalized by the transducer bandwidth in the frequency domain in order to remove the influence of the transducer bandwidth, wall-filtered to remove echoes from the cellulose tube, then bandpass-filtered ($7^{th}$ order Butterworth, 50% bandwidth). Filtering and analysis were performed using Matlab (The Mathworks, Natick, MA). Videos of optical data were reviewed in ImageJ (Version 1.47, NIH, Bethesda, MD) to assess bubble fragmentation and to measure the change in diameter. Any bubble decreasing in diameter by at least 10% of its original value was categorized as shrinking. Because our goal is to reliably perform imaging of broadband superharmonic signals, this three category classification system (no change in diameter, shrinking bubble, immediate fragmentation) is helpful in determining whether harmonic-producing bubbles persist over multiple pulses.

Logistic regression analysis was performed in Matlab to determine the thresholds for bubble fragmentation and shrinking as a function of frequency and pressure and as a function of diameter and pressure as in Chomas et al. (Chomas et al. 2001b). For determining the fragmentation threshold, a binomial distribution was used and each observed bubble was classified as either immediately fragmenting (i.e on the first pulse) or non-fragmenting. For determining the shrinking threshold, each observed bubble was classified as either shrinking

Author Manuscript Author Manuscript Author Manuscript Author Manuscript

(by at least 10% on the first pulse) or non-shrinking. The slope of the fit line given by the generalized linear model (glmfit) was also computed in Matlab.

### Dual-frequency imaging of stationary microbubbles

In order to directly assess the role of shell fragmentation in broadband superharmonic signal generation in populations of bubbles, solutions containing $10^7$ bubbles/mL of either 1 or 4 μm microbubbles were injected into a 200 μm cellulose tube in a water bath positioned at the focus (1.5 cm) of a custom mechanically-steered dual-frequency transducer having a 4 MHz transmit and a 30 MHz receiving element (Gessner et al. 2010). This custom probe was connected to a VisualSonics Vevo 770 high frequency imaging system (Toronto, Canada) which has been modified to transmit using an external waveform generator (Tektronix AWG2021) and amplifier (ENI 3100 LA, Rochester, NY) while forming images only containing high frequency signal content > 15 MHz (in-line highpass filter, TTE, Los Angeles, CA). The flow was allowed to stabilize for 10 minutes to ensure minimal redistribution of bubbles into or out of the tube at the time of image acquisition. Imaging was then performed using a single-cycle 4 MHz pulse at a frame rate of 1 Hz for 50 frames; image sequences were stored to analyze image brightness as a function of frame rate. This test was performed three times at each peak negative pressure from 275 to 400 kPa in 25 kPa increments. Acquired images were processed by subtracting a control image containing only the cellulose tube filled with water from each frame of each experimental acquisition (Version 1.47, ImageJ, NIH, Bethesda, MD). A region of interest (ROI) of identical size and location was then drawn over the resulting images and average brightness within the ROI was computed for each frame.

### In vivo dual-frequency imaging

While *in vitro* imaging analysis of stationary bubbles provides insight into fragmentation or shrinking behaviors over time, there are no stationary bubbles when imaging *in vivo*, and thus the feasibility of any high-frame rate imaging technique which may induce either shell rupture or fragmentation depends on the relationship between bubble destruction rate and local perfusion rates. For this reason, bubble destruction was assessed *in vivo* by imaging two rodents at two distinct frame rates (4 and 7 Hz) for each animal, thus varying the rate of any destructive processes with respect to the perfusion rate. Two healthy Fischer 344 rats were imaged using the custom dual-frequency probe described previously and the VisualSonics Vevo 770 with a region of interest centered on the kidney. Animals were depilated and scanned while under isoflurane anesthesia according to a protocol approved by the Animal Care and Use Committee of the University of North Carolina. Contrast agent ($3.3\times10^9$ bubbles/mL, 1 μm diameter) was infused continuously at a rate of 40 μL/min. Peak negative pressure was varied up to 1300 kPa, ensuring MI remained below 0.7. Note that actual pressure at the focus was less than that measured in water pressure due to attenuation. Images were analyzed by comparing average brightness within an identical ROI containing the kidney for each acquired frame. Frames containing motion artifacts due to respiration were discarded in order to compare the same anatomical region over time.

Author Manuscript Author Manuscript Author Manuscript Author Manuscript

# RESULTS

## Optical observation of fragmentation threshold

Results of bubble behavior in optical observations are reported for each pressure-frequency combination in Figure 4A and for each pressure-diameter combination in Figure 4B. In Fig. 4A, the fragmentation threshold (dashed line) increases with frequency as previously reported (Chomas et al. 2001b; Chen et al. 2003; Yeh and Su 2008) with a slope of 36 kPa/MHz, with $p<.0001$ for pressure and $p<.005$ for frequency. Experiments indicate there is no relationship between frequency and the threshold for bubble shrinking ($p=0.63$). This may be due to the use of a range of transmit frequencies which are lower than expected bubble resonance, i.e. native Definity® exhibits resonance at approximately 10 MHz for 1.1–3.3 μm mean bubble diameter (Goertz et al. 2007). However, use of lower frequencies is necessary for superharmonic imaging.

Bubble shrinking is observed predominantly in larger bubbles at moderate pressures (approximately 300 kPa). In Fig. 4B, the dashed line shows the fragmentation threshold (slope 36 kPa/μm, pressure: $p<.0001$, diameter: $p<.005$) and the solid line represents the shrinking threshold (slope −18 kPa/μm, pressure: $p<.0001$, diameter: $p<.0001$). While other researchers have previously reported preferential shrinking in smaller bubbles at peak pressures less than 100 kPa (Guidi et al. 2010), shrinking was not observed in small bubbles in this study.

## Tracking single bubbles through simultaneous optical/acoustic measurements

In order to further illustrate the individual bubble responses within the described three categories, we present exemplary optical images and corresponding spectra for each of the seven different cases of bubble behavior observed. Each sequence of optical images depicts the microbubble as it appeared before pulse delivery and after the delivery of each of five pulses.

In Fig. 5A, a 1 μm bubble exhibits no change in diameter and very similar spectra in response to five consecutive pulses at 3.75 MHz and a peak negative pressure of 300 kPa. In Fig. 5B, a bubble shrinks once, then remains stable to subsequent pulses. Within this sequence of pulses, acoustic signals having the highest amplitude are observed when the bubble shrinks. After the second pulse, the peak occurs at a higher frequency, then slowly shifts downward with subsequent pulses, although no further change in diameter is visible. Multiple discrete shrinking events were often observed for larger bubbles, as exemplified in Fig. 5C for a 4 μm bubble at 1.75 MHz and a peak negative pressure of 200 kPa. In this figure, a decrease in microbubble diameter may be observed after each successive pulse, with the strongest superharmonic signals recorded after the first and second shrinking events.

At sufficiently high pressures or low frequencies, microbubble shells visibly fragmented on the first pulse, producing a single strong echo on the first pulse alone (Fig. 5D, 1.75 MHz, 500 kPa). Meanwhile, unique responses were observed at intermediate frequencies and pressures, including multiple shrinking events followed by either bubble disappearance without visible shell fragmentation (Fig. 5E) or shell fragmentation (Fig. 5F). While shell

Author Manuscript Author Manuscript Author Manuscript Author Manuscript

fragmentation was not visible in all cases (Fig. 5G), even in its absence, strong broadband echoes may be present (Pulse 5, Fig. 5E) as core gas is lost. In our study, bubble fragmentation occurred with larger bubbles for both the initial bubble (Pulse 4, Fig. 5F) and smaller remnant bubbles (Pulse 5, Fig. 5G). Fragmentation of these daughter bubbles produced a strong broadband signal similar to a shrinking event in a large bubble (compare responses to Pulses 2 and 5, Fig. 5G) but weaker than fragmentation of a single small bubble (Pulse 1, Fig. 5D). In some cases, the original bubble produced one or more stable daughter bubbles on the first pulse (Fig. 5G). The formation of daughter bubbles was observed only in 4 μm bubbles and in the following cases: in 1 of 25 acquisitions at 300 kPa, and 7 of 25 acquisitions at 400 kPa. The presence of a daughter bubble can be seen to produce two spectral peaks (Fig. 5G), with one bubble remaining stable to subsequent pulses.

### Single bubble observations

Optical observations reveal the existence of many different cases of bubble dissolution which fall within the category of “shrinking” used in the analysis in Fig. 4. In order to fully display all types of bubble behavior and the conditions under which they occur, these subcategories of shrinking bubbles are presented in full in Fig. 6. However, the three simple categories indicating no change in bubble diameter, >10% decrease in bubble diameter, and complete shell fragmentation are useful for assessing superharmonic signal generation and the duration of the effect. In Fig. 7A, the mean spectra after the first pulse are displayed for three categories of observed behavior: bubbles which show no change in diameter, shrinking bubbles, and bubbles with complete shell fragmentation. A fragmenting bubble produces the strongest response, while a shrinking bubble produces a far weaker superharmonic signal containing approximately 25% of the energy of the fragmenting bubble. A bubble exhibiting no change in diameter produces superharmonic energy nearly equal to the control case in which no bubble was present. The persistence of this superharmonic content over five pulses is displayed in Fig. 7B, where the energy resulting from the shrinking bubble case—initially approximately 25% of the energy from fragmenting bubbles—remains relatively constant over five pulses but is relatively similar to the case of the unchanging bubble diameter. Both the shrinking bubble and unchanging diameter cases produce greater amplitude than the control case (no bubble present), suggesting that weak harmonic signals may be produced in some cases due to events which results in little loss of core gas.

In additional experiments at each of two frequency-pressure combinations (1.75 MHz, 200 and 300 kPa, n=2 single bubble trials each case) designed to investigate a bubble’s ability to produce superharmonic energy over 50 pulses as in real-time imaging, bubbles were observed to shrink to a stable diameter and to continually emit low levels of superharmonic energy. Single results for 1.75 MHz, 200 and 300 kPa pulses are shown in Figure 8. Guidi et al. reported continued microbubble scattering at the transmitted frequency after deflation but did not examine harmonic response (Guidi et al. 2010). In investigating non-spherical oscillations next to a wall, Vos et al. report a high degree of correlation between the second harmonic and the occurrence of microjetting, noting that the presence of a jet did not always coincide with instantaneous microbubble destruction (Vos et al. 2007).

Author Manuscript Author Manuscript Author Manuscript Author Manuscript

### Dual-frequency imaging of stationary microbubbles

Results for dual-frequency imaging experiments with stationary bubbles in a tube at peak negative pressures of 300, 350, and 400 kPa are shown in Fig. 9. At 300 kPa, there is a decrease in image brightness of 1 μm bubbles during the first ten frames, followed by a slower decline over the remaining frames. 4 μm bubbles exhibit only a very weak decrease in brightness, though brightness remains well below that of 1 μm bubbles. This is consistent with the fact that the fragmentation threshold increases with bubble diameter, and that signals which coincide with bubble deflation have demonstrated lower harmonic amplitudes in this study and lower amplitudes at the transmitted frequency in previous studies (Vos et al. 2007). At 350 kPa, image brightness declines exponentially for 1 μm bubbles, ending at a level similar to that of 4 μm bubbles. 4 μm bubbles again exhibit little decrease with respect to time at 350 kPa. At 400 kPa, bubbles of both sizes show a rapid decrease in brightness over the first 5 frames, after which 4 μm bubbles stabilize and 1 μm bubbles exhibit a slow decline in image brightness. Final image brightness for 4 μm bubbles exceeds that of 1 μm bubbles at 400 kPa.

Collectively, these results suggest that generation of a broadband superharmonic response is dependent on microbubble oscillation resulting in destructive processes—either immediate fragmentation with $p < 0.0001$ for pressure, $p < 0.005$ for diameter and $p < 0.005$ for frequency, or shell rupture and microbubble deflation with $p < 0.0001$ for pressure, $p < 0.0001$ for diameter, and no significant frequency dependence—although some image intensity remains even after 50 frames in all cases involving microbubble populations (control images of tubes were subtracted). This might be explained by the stability of deflated bubbles, which has been directly observed in this study and previously (Guidi et al. 2010). Results also indicate that in populations of microbubbles, minimal fragmentation (or harmonic generation) occurs for 4 μm bubbles below approximately 400 kPa.

### In vivo dual-frequency imaging

Mean image intensity for an ROI containing the kidney averaged over both animals is plotted as a function of frame number at pressures of 700, 1000, and 1300 kPa in Fig. 10. For each pressure, the final image is displayed for both 4 Hz and 7 Hz cases. At a nominal peak negative pressure of 700 kPa (Fig. 10A), both frame rates show very little decline in brightness over time, and final images are very similar. At a nominal peak negative pressure of 1000 kPa (Fig. 10B), mean brightness of images acquired at 4 Hz is observed to settle to a higher value (20) than those acquired at 7 Hz (15). Finally, at a nominal peak negative pressure of 1300 kPa, both frame rates exhibit a greater initial intensity and a more rapid decline from that initial intensity (Fig. 10C) than at 1000 kPa, with image intensity for both frame rates settling to similar values. At higher pressures, lower frame rates allowed for an increase in perfusion relative to destruction, increasing steady-state image brightness by 27% at 1000 kPa (Figure 10B) and 29% at 1300 kPa (Figure 10C).

## DISCUSSION

In this work, we have described superharmonic signals generated by 1 and 4 μm lipid-shelled bubbles with simultaneous optical observation in order to determine the origin of

Author Manuscript Author Manuscript Author Manuscript Author Manuscript

these signals. The broadband harmonic signal most commonly associated with superharmonic imaging was observed when significant shell fragmentation occurred on the first pulse and was absent on subsequent pulses (Fig. 7). Larger microbubbles had a slightly higher fragmentation threshold (Fig. 4B) and were observed to shrink at pressures below this threshold, producing weaker superharmonic signals (Fig. 7A) persisting over many pulses (Fig. 7B, Fig. 8). Likelihood of shrinking was found to increase with initial bubble diameter (Fig. 4B). While multiple discrete shrinking events were observed in some cases (Fig. 5C), at moderate pressures bubbles shrank to a stable size—which is consistent with previous studies (Borden et al. 2005)—then maintained a constant diameter and emitted constant, weak harmonic echoes with subsequent pulses. The production of weak superharmonic signals by bubbles which did not visibly shrink or fragment raises the question of whether lipid shedding or “nanofragmentation” reported by other researchers may be occurring in these cases (Borden et al. 2005; Yasui et al. 2009; Cox and Thomas 2013). One of these previous studies also showed that increasing shell cohesiveness by using longer lipid chain lengths decreased the rate of microbubble dissolution (Borden et al. 2005), which may be useful in prolonging the weaker subharmonic signal observed in the presence of shrinking of events. It is unclear what sensitivity might be required in order to detect this signal *in vivo* in the presence of attenuation, however, the persistence of detectable microbubble signals to 50 frames in tube imaging indicates that in the presence of adequate microbubble concentrations, the superposition of deflation signals can be detected with a prototype imaging system.

### Role of shell fragmentation in superharmonic signal production

The strongest, most broadband harmonic signals were present when shell fragmentation occurred on the initial pulse (Fig. 5D). However, there are still significant harmonic signals produced in cases of sub-threshold pressures (Figs. 5B–C) which are quite different in nature from the spectra observed when the shell is fragmented on the first pulse (Fig. 5D). If the superharmonic signal were to occur solely due to shell fragmentation, there would be no harmonic signal produced by sub-threshold pulses. This suggests that although superharmonic signal production is often associated with shell fragmentation, end state fragmentation may not be required. One possible explanation is the occurrence of transient fragmentation events which are followed by bubbles re-forming (Biagi et al. 2007). Because shell rupture can occur at pressures lower than those required for stable or inertial cavitation (Haworth et al. 2012), release of core gas is not necessarily indicative of stable or inertial cavitation. A stable cavitation threshold for Definity® of 0.42 MPa has been reported for 10 cycle pulses at 6 MHz, as determined by the presence of subharmonic emissions (Porter et al. 2006) (Coussios et al. 2007). A lower threshold may be expected at the reduced frequencies used in our study, though the use of shorter pulses should slightly increase cavitation thresholds. Ultimately, since the generated echo response is a function of the bubble radius, wall velocity, and wall acceleration (Leighton 1994; Dayton et al. 1999), it is likely that the actual source of broadband energy generation cannot be observed on the time and spatial resolution scales observed in our optical experiments.

The presence of harmonic content at a level above the control level even in the absence of observable shell fragmentation (Figs. 7A–B) indicates that the weaker superharmonic

Author Manuscript Author Manuscript Author Manuscript Author Manuscript

signals are produced when bubbles shrink without complete bubble fragmentation, though shell damage is required to facilitate the observed rapid loss of core gas. The exact mechanism by which ultrasound induces microbubble deflation is unknown, though it has been hypothesized that lipid shedding produces an increase in surface tension and subsequently in Laplace pressure, resulting in gas dissolution (Datta et al. 2008). While the role of sub-resolution lipid shedding or fluid turbulence without apparent loss of core gas cannot be determined without further study, these phenomena may help explain the presence of superharmonic signals produced by bubbles with stable diameters. The fact that the optical field of view was smaller than the acoustic beam diameter allows for the possibility that additional unobservable microbubbles may have been present within the receive beam. With increasing distance from the center of the focus, these additional microbubbles would experience decreased pressures under the transmit beam and also contribute diminishing echoes to the received signals relative to the optically-observed, on-axis microbubble. If present, contributions from additional, off-axis microbubbles under the focus would sum constructively, increasing the amplitude of acquired signals, though in a constant manner across all cases tested because dilutions were equivalent.

Finally, in analyzing fragmentation and shrinking thresholds, it was difficult to ascertain a frequency threshold for shrinking. If bubble fragmentation is an effect of inertial cavitation and dependent primarily on fluid motion surrounding the bubble, while bubble shrinking is a stable cavitation effect and thus dependent on individual bubble properties such as the coating (Radhakrishnan et al. 2013), this may explain the presence of a clear fragmentation threshold for fragmentation but not for shrinking.

### Effect of bubble diameter on superharmonic signal production

In previous work, we observed an increase in superharmonic scattering for 4 μm bubbles at lower pressures (approximately 300–500 kPa) relative to that of 1 μm bubbles at the same pressures (Lindsey et al. 2014). There are two possible explanations for this phenomenon: 1) Larger bubbles have a larger scattering cross section, resulting in greater energy returning to the transducer, and 2) As observed in these experiments, larger bubbles are more prone to shrinking than smaller bubbles, which produces a weak superharmonic signal. At peak pressures less than 500 kPa, many large bubbles do not fragment but rather become smaller bubbles, which may in turn fragment on subsequent pulses, prolonging the harmonic signal for a greater number of pulses and thus increasing the 4 μm harmonic signal. In dual-frequency imaging of populations of stationary bubbles in a tube, image intensity for 4 μm bubbles exceeded that of 1 μm bubbles at 400 kPa (Fig. 9), when bubbles may be expected to fragment rapidly.

### Superharmonic imaging of populations of microbubbles in a tube

The results of imaging stationary microbubbles in tubes indicate that only a limited decrease in image brightness occurs over time at peak negative pressures of 300 and 350 kPa and that some superharmonic signal content is produced even after 50 pulses. There are several possible explanations for this prolonged lifespan of bubbles: 1) bubbles at the back of the tube are shielded by those at the front during initial pulses until shielding bubbles are gradually destroyed in a front-to-back progression; 2) most individual bubbles are observed

Author Manuscript Author Manuscript Author Manuscript Author Manuscript

to shrink at 300 kPa (Fig. 4B), resulting in many bubbles producing the weak superharmonic signal observed in Figure 7A on each pulse; 3) larger bubbles shrink until reaching a diameter at which they are small enough to be destroyed. The accumulation of excess shell material could also affect the stability of shrinking bubbles, though this would require further study. Nonetheless, the sharp decline in image intensity observed over the first 10 frames for 1 μm bubbles indicates that many small bubbles are destroyed during the first few frames. This rapid decrease in image brightness during initial frames is not observed for 4 μm bubbles until pressure is increased to 400 kPa, suggesting that their stable superharmonic content at lower pressures is the result of the dissolution behavior (shrinking) observed in single bubble experiments. That 400 kPa is sufficient to destroy some larger bubbles is also consistent with single bubble observations (Fig. 4B).

### In vivo superharmonic imaging

When performing *in vivo* imaging, much higher peak pressures were required to generate sufficient superharmonic signal content to provide adequate contrast in images. No contrast was visible below 500 kPa; the 700 kPa images shown represent the approximate lower bound of superharmonic imaging *in vivo* using the described system (Fig. 10A). The requirement of higher pressure may be explained by both attenuation and small vessel confinement effects *in vivo*. For example, for an imaging depth of 1.5 cm, an attenuation of 0.2 dB/cm/MHz in overlying tissues represents a loss of 1.2 dB at 4 MHz. Superharmonic echoes may be expected to be difficult to detect at the transducer due to the strong attenuation of high frequency waves. For example, attenuation of 0.2 dB/cm/MHz results in attenuations of 9 dB at 30 MHz. Caskey et al. have also reported that microbubble oscillation is constrained when bubbles are confined to smaller vessels, which may indicate higher pressures are required to produce superharmonic signals in small vessels (Caskey et al. 2007). However, reduced bubble expansion *in vivo* was also associated with an increased oscillation lifetime and a change in the destruction mechanism from fragmentation to acoustically-driven diffusion.

Peak negative pressures greater than 500 kPa were needed to reliably produce images *in vivo*. The increased image contrast at 1000 and 1300 kPa was greatly preferred for diagnostic use relative to the 700 kPa images. These images at higher peak pressures also exhibited a decrease in image intensity with respect to frame number. This re-affirms the notion that some form of bubble destruction—whether through formation of small shell discontinuities or shell fragmentation—is necessary to produce superharmonic signal content. At these higher pressures, lower frame rates allowed for an increase in perfusion relative to destruction, (Figure 10B–10C). Taken in aggregate, these *in vivo* imaging results demonstrate that the images having the highest contrast are produced on the initial frame(s), but also that steady-state contrast can be increased by decreasing frame rate. However, in imaging the rodent kidney, the re-perfusion rate was high enough that useful images were still acquired at 7 Hz even after many frames. Because only relatively low frame rates could be tested due to system limitations imposed by a mechanically-steered transducer, superharmonic imaging may face greater challenges if frame rates were to be increased further. It should also be noted that larger vessels typically have faster flow rates, indicating

Author Manuscript Author Manuscript Author Manuscript Author Manuscript

that increasing frame rate may decrease contrast to smallest vessels, effectively decreasing resolution by eliminating the ability to distinguish the smallest features.

## Implications for imaging

The results presented indicate that in order to produce a high-amplitude, broadband harmonic signal, a combination of frequency, pressure, and bubble diameter that will result in bubble dissolution via either shrinking or shell fragmentation should be utilized. The map of bubble destruction behaviors in Fig. 6 provides initial guidance as to the pressure that may be used to induce different behavior in a microbubble of a given diameter, information which could be useful in either imaging or drug delivery. For instance, if the goal is to induce as many multiple shrinking events as possible, one might use 300–400 kPa pulses with 3–4 μm bubbles (Fig. 6). If the goal is simply to avoid fragmentation (i.e. for bioeffects considerations or in dual-frequency molecular imaging), one might use bubbles at least 3 μm in diameter while maintaining focal pressures below 400 kPa *in vitro* (or the diameter-pressure combination inducing the equivalent regime *in vivo*). Achieving the desired focal pressure during *in vivo* imaging would require prior transducer calibration in water followed by estimation of attenuation, aberration, and vessel wall effects (Caskey et al. 2007; Couture et al. 2009; Doinikov et al. 2009). The presented single bubble studies also ignored effects of multiple scattering, which plays an important role during *in vivo* imaging, particularly as microbubble concentrations and peak pressures increase (Porter et al. 2006; Haworth et al. 2012).

While broadband superharmonic signals arising from shell fragmentation are necessarily short-lived, results suggest that by increasing frequency or increasing bubble diameter, it may instead be possible to reliably produce weaker harmonics having a longer duration over multiple pulses. *In vivo* results also indicate that perfusion, at least in the rodent case, is sufficient as to produce minimal loss in contrast at frame rates up to 7 Hz even with 1 μm bubbles. In the case of high local perfusion rates, that is when there is significant bubble motion under the point spread function (PSF) between pulse repetition intervals, immediate shell fragmentation is likely most desirable. However, when microbubble motion under the PSF is minimal during a single pulse repetition interval (as may be the case in the smaller vessels), superharmonic imaging may be prolonged and diagnostic efficacy improved by transmitting at sub-threshold pressures for a given microbubble population. This consideration will become more important as dual-frequency imaging systems with increasing frame rates are developed and *in vivo* application of this technology is further investigated.

Microbubble dissolution in superharmonic imaging carries further implications for functional imaging approaches. In investigating microbubble dissolution after disruption, Couture et al. utilized high-frame rate B-mode imaging to observe differences in microbubble dissolution over the cross-section of a vessel. They suggested that “rapid B-mode imaging might provide new information on the geometry and the local environment of bubble clouds” (Couture et al. 2009). Dissolution curves in superharmonic imaging might yield similar information at a higher resolution. For this reason, understanding the mechanism of broadband superharmonic signal production could enable identification of

Author Manuscript Author Manuscript Author Manuscript Author Manuscript

small variations in the vascular environment in addition to allowing for optimization of acoustic angiography imaging.

Additionally, in molecular imaging only a small number of microbubbles adhere to a pathology site (Talu et al. 2007), making it important to optimize the imaging system's ability to detect microbubbles without destroying them. While using larger microbubbles would further reduce the total number of microbubbles able to bind to a site, these results suggest that the use of true (rather than nominal) focal pressures less than approximately 400 kPa and accounting for confinement effects may allow superharmonic imaging of targeted microbubbles without immediate shell fragmentation.

For any microbubble-based ultrasound imaging approach, mechanical bioeffects must also be considered. Researchers have observed the formation of micro fluidic jets or "microjets" at pressures in the diagnostic range (Coussios et al. 2007; Datta et al. 2008). Microjetting has previously been characterized by the presence of subharmonic echoes (i.e. stable cavitation) (Datta et al. 2008). While previous studies have reported the presence of microjetting at microbubble sizes and pressures similar to those used in this work (Skyba et al. 1998; Zhao et al. 2005; Vos et al. 2007), we are unable to comment on the presence of this effect at this time, as the camera used in this work does not have adequate temporal resolution to observe microjetting. However, if microjetting does in fact occur, which seems likely for cases involving higher peak pressures and smaller microbubbles, then there could be biological effect considerations for bubbles close to a wall, which experience asymmetric oscillation and microjetting which may result in cell damage (Thieme and Shung 1992). If utilizing lower peak pressure and larger microbubbles allows for superharmonic signal production based on shell rupture or shedding rather than cavitation, this may provide an alternative path for superharmonic imaging with potentially less biological interaction. Regardless, it is important to note that the pressure requirements to cause superharmonic signal generation as observed here are higher than that used for "low-MI" clinical imaging (Kim et al. 2008), yet still below the maximum mechanical index of 0.8 for which safety has been evaluated for Definity® (Lantheus Medical Imaging, N. Billerica, MA) (Imaging 2013). Furthermore, the 'flash' technique of clearing microbubbles which causes microbubble fragmentation is a high-MI technique (up to 1.9) utilizing short bursts of acoustic pressures greater than tested here, has been used for over a decade regularly in clinical myocardial perfusion imaging without noted adverse effects (Aggeli et al. 2008; Dolan et al. 2009).

### Implications of microbubble shell

The influence of shell properties in lipid-shelled microbubbles has been previously described (Borden et al. 2005). Alternatively, polymer-shelled bubbles have demonstrated a fragmentation threshold which is at least 500 kPa higher than that of lipid-shelled bubbles. However, polymer-shelled bubbles are less prone to acoustically-driven changes in diameter (Bloch et al. 2004), which would seem to make them a poor choice for producing superharmonic signals. The observed mechanism of destruction in polymer-shelled bubbles is also different from lipid-shelled bubbles, as the formation of a single defect has been observed in the polymer shell through which core gas escapes at a very high velocity to form

Author Manuscript Author Manuscript Author Manuscript Author Manuscript

a daughter bubble. As the presented results suggest that shell rupture, often accompanied by loss of core gas, is associated with superharmonic signal generation, a single shell rupture event might be expected to produce a single discrete signal rather than the repeated signals observed with shrinking bubbles. However, mechanisms of signal production in polymer shells may be entirely different from those in lipid shells, as polymer shells exhibit sonic cracking due to high surface tension, while lipid shells do not exhibit sonic cracking, only lipid shedding. Finally, protein shells (i.e. albumin), are also more rigid than lipid shells and have been shown to produce echoes of increasing amplitude over repeated pulsing when transmitting at 2.25 MHz and receiving first harmonic echoes at 5 MHz (Dayton et al. 1999). Optical observations of the same albumin-shelled microbubbles indicate that these echoes are associated with asymmetrical shell buckling and loss of rigidity, which may be useful phenomena for the production of superharmonic signals. Previous studies have reported the presence of narrowband harmonics when using albumin-shelled microbubbles (Shi et al. 1999; Shi and Forsberg 2000).

## CONCLUSIONS

In this work, the role of bubble destruction in superharmonic signal production was investigated through simultaneous optical and acoustic measurements at transmit frequencies from 1.75 to 3.75 MHz and pressures near the shell fragmentation threshold for 1 and 4 μm bubbles. Results indicate that superharmonic signals having the broadest bandwidth and highest energy are associated with shell fragmentation, which preferentially occurs for smaller bubbles at lower frequencies and higher pressures. However, a superharmonic signal is still produced from bubbles which are not fragmented, which has the potential to prolong the life and imaging efficacy of microbubbles or reduce the peak pressures required at the cost of reduced amplitude relative to the microbubble fragmentation case. Populations of 1 μm bubbles exhibited faster dissolution relative to 4 μm bubbles in dual-frequency imaging of stationary bubbles. Increasing frame rate from 4 to 7 Hz during *in vivo* imaging in rodents decreased mean steady-state image brightness by 27% at 1000 kPa and 29% at 1300 kPa. Considerations of peak negative pressures and frame rate will take on added significance for the development of real-time *in vivo* superharmonic imaging systems.

## Acknowledgments

This work was supported by grant R01CA170665 from the National Institutes of Health. The authors thank Jim Tsuruta for guidance with contrast agent preparation, Jillian Weigel for preparing lipid solution, Sarah Shelton for helpful conversations, and Kennita Johnson and Paul Sheeran for assistance with the high speed camera acquisition system.

## References

Aggeli C, Giannopoulos G, Roussakis G, Christoforatou E, Marinos G, Toli C, Pitsavos C, Stefanadis C. Safety of myocardial flash-contrast echocardiography in combination with dobutamine stress testing for the detection of ischaemia in 5250 studies. Heart. 2008; 94:1571–7. [PubMed: 18474538]

Ammi AY, Cleveland RO, Mamou J, Wang GI, Bridal SL, O'Brien WD Jr. Ultrasonic contrast agent shell rupture detected by inertial cavitation and rebound signals. IEEE transactions on ultrasonics, ferroelectrics, and frequency control. 2006; 53:126–36.

Author Manuscript Author Manuscript Author Manuscript Author Manuscript

Biagi E, Breschi L, Vannacci E, Masotti L. Stable and transient subharmonic emissions from isolated contrast agent microbubbles. IEEE transactions on ultrasonics, ferroelectrics, and frequency control. 2007; 54:480–97.

Bloch SH, Wan M, Dayton PA, Ferrara KW. Optical observation of lipid- and polymer-shelled ultrasound microbubble contrast agents. Appl Phys Lett. 2004; 84:631–3.

Borden MA, Kruse DE, Caskey CF, Zhao S, Dayton PA, Ferrara KW. Influence of lipid shell physicochemical properties on ultrasound-induced microbubble destruction. IEEE transactions on ultrasonics, ferroelectrics, and frequency control. 2005; 52:1992–2002.

Bouakaz A, Krenning BJ, Vletter WB, ten Cate FJ, De Jong N. Contrast superharmonic imaging: a feasibility study. Ultrasound Med Biol. 2003; 29:547–53. [PubMed: 12749924]

Bouakaz A, Versluis M, de Jong N. High-speed optical observations of contrast agent destruction. Ultrasound Med Biol. 2005; 31:391–9. [PubMed: 15749563]

Brawer MK, Deering RE, Brown M, Preston SD, Bigler SA. Predictors of pathologic stage in prostatic carcinoma. The role of neovascularity Cancer. 1994; 73:678–87. [PubMed: 7507798]

Bullitt E, Wolthusen PA, Brubaker L, Lin W, Zeng D, Van Dyke T. Malignancy-associated vessel tortuosity: a computer-assisted, MR angiographic study of choroid plexus carcinoma in genetically engineered mice. AJNR American journal of neuroradiology. 2006; 27:612–9. [PubMed: 16552004]

Casey J, Sennoga C, Mulvana H, Hajnal JV, Tang MX, Eckersley RJ. Single bubble acoustic characterization and stability measurement of adherent microbubbles. Ultrasound Med Biol. 2013; 39:903–14. [PubMed: 23473537]

Caskey CF, Stieger SM, Qin S, Dayton PA, Ferrara KW. Direct observations of ultrasound microbubble contrast agent interaction with the microvessel wall. Journal of the Acoustical Society of America. 2007; 122:1191–200. [PubMed: 17672665]

Chang PH, Shung KK, Wu SJ, Levene HB. Second harmonic imaging and harmonic Doppler measurements with Albunex IEEE transactions on ultrasonics, ferroelectrics, and frequency control. 1995; 42:1020–7.

Chang PP, Chen WS, Mourad PD, Poliachik SL, Crum LA. Thresholds for inertial cavitation in albunex suspensions under pulsed ultrasound conditions. IEEE transactions on ultrasonics, ferroelectrics, and frequency control. 2001; 48:161–70.

Chen WS, Matula TJ, Brayman AA, Crum LA. A comparison of the fragmentation thresholds and inertial cavitation doses of different ultrasound contrast agents. The Journal of the Acoustical Society of America. 2003; 113:643–51. [PubMed: 12558300]

Chen WS, Matula TJ, Crum LA. The disappearance of ultrasound contrast bubbles: observations of bubble dissolution and cavitation nucleation. Ultrasound Med Biol. 2002; 28:793–803. [PubMed: 12113792]

Chomas JE, Dayton P, Allen J, Morgan K, Ferrara KW. Mechanisms of contrast agent destruction. IEEE transactions on ultrasonics, ferroelectrics, and frequency control. 2001a; 48:232–48.

Chomas JE, Dayton P, May D, Ferrara K. Threshold of fragmentation for ultrasonic contrast agents. Journal of biomedical optics. 2001b; 6:141–50. [PubMed: 11375723]

Coussios CC, Farny CH, Ter Haar G, Roy RA. Role of acoustic cavitation in the delivery and monitoring of cancer treatment by high-intensity focused ultrasound (HIFU). Int J Hyperther. 2007; 23:105–20.

Couture O, Bannouf S, Montaldo G, Aubry JF, Fink M, Tanter M. Ultrafast imaging of ultrasound contrast agents. Ultrasound Med Biol. 2009; 35:1908–16. [PubMed: 19699026]

Cox DJ, Thomas JL. Ultrasound-induced dissolution of lipid-coated and uncoated gas bubbles. Langmuir : the ACS journal of surfaces and colloids. 2010; 26:14774–81. [PubMed: 20722377]

Cox DJ, Thomas JL. Rapid shrinkage of lipid-coated bubbles in pulsed ultrasound. Ultrasound Med Biol. 2013; 39:466–74. [PubMed: 23245826]

Datta S, Coussics CC, Ammi AY, Mast TD, de Courten-Myers GM, Holland CK. Ultrasound-enhanced thrombolysis using Definity (R) as a cavitation nucleation agent. Ultrasound in Medicine and Biology. 2008; 34:1421–33. [PubMed: 18378380]

Dayton PA, Morgan KE, Klibanov AL, Brandenburger GH, Ferrara KW. Optical and acoustical observations of the effects of ultrasound on contrast agents. IEEE transactions on ultrasonics, ferroelectrics, and frequency control. 1999; 46:220–32.

Author Manuscript Author Manuscript Author Manuscript Author Manuscript

Doinikov AA, Zhao S, Dayton PA. Modeling of the acoustic response from contrast agent microbubbles near a rigid wall. Ultrasonics. 2009; 49:195–201. [PubMed: 18789469]

Dolan MS, Gala SS, Dodla S, Abdelmoneim SS, Xie F, Cloutier D, Bierig M, Mulvagh SL, Porter TR, Labovitz AJ. Safety and efficacy of commercially available ultrasound contrast agents for rest and stress echocardiography a multicenter experience. Journal of the American College of Cardiology. 2009; 53:32–8. [PubMed: 19118722]

Duff SE, Jeziorska M, Kumar S, Haboubi N, Sherlock D, O'Dwyer ST, Jayson GC. Lymphatic vessel density, microvessel density and lymphangiogenic growth factor expression in colorectal cancer. Colorectal Dis. 2007; 9:793–800. [PubMed: 17931169]

Everbach EC, Makin IR, Azadniv M, Meltzer RS. Correlation of ultrasound-induced hemolysis with cavitation detector output in vitro. Ultrasound Med Biol. 1997; 23:619–24. [PubMed: 9232771]

Feshitan JA, Chen CC, Kwan JJ, Borden MA. Microbubble size isolation by differential centrifugation. Journal of colloid and interface science. 2009; 329:316–24. [PubMed: 18950786]

Fox SB, Leek RD, Weekes MP, Whitehouse RM, Gatter KC, Harris AL. Quantitation and prognostic value of breast cancer angiogenesis: comparison of microvessel density, Chalkley count, and computer image analysis. J Pathol. 1995; 177:275–83. [PubMed: 8551390]

Gessner R, Lukacs M, Lee M, Cherin E, Foster FS, Dayton PA. High-resolution, high-contrast ultrasound imaging using a prototype dual-frequency transducer: in vitro and in vivo studies. IEEE transactions on ultrasonics, ferroelectrics, and frequency control. 2010; 57:1772–81.

Gessner RC, Aylward SR, Dayton PA. Mapping microvasculature with acoustic angiography yields quantifiable differences between healthy and tumor-bearing tissue volumes in a rodent model. Radiology. 2012; 264:733–40. [PubMed: 22771882]

Gessner RC, Frederick CB, Foster FS, Dayton PA. Acoustic angiography: a new imaging modality for assessing microvasculature architecture. International journal of biomedical imaging. 2013; 2013:936593. [PubMed: 23997762]

Goertz DE, de Jong N, van der Steen AF. Attenuation and size distribution measurements of Definity and manipulated Definity populations. Ultrasound Med Biol. 2007; 33:1376–88. [PubMed: 17521801]

Guidi F, Vos HJ, Mori R, de Jong N, Tortoli P. Microbubble characterization through acoustically induced deflation. IEEE transactions on ultrasonics, ferroelectrics, and frequency control. 2010; 57:193–202.

Haworth KJ, Mast TD, Radhakrishnan K, Burgess MT, Kopechek JA, Huang SL, McPherson DD, Holland CK. Passive imaging with pulsed ultrasound insonations. The Journal of the Acoustical Society of America. 2012; 132:544–53. [PubMed: 22779500]

Kim TK, Jang HJ, Burns PN, Murphy-Lavallee J, Wilson SR. Focal nodular hyperplasia and hepatic adenoma: differentiation with low-mechanical-index contrast-enhanced sonography. AJR American journal of roentgenology. 2008; 190:58–66. [PubMed: 18094294]

King DA, Malloy MJ, Roberts AC, Haak A, Yoder CC, O'Brien WD Jr. Determination of postexcitation thresholds for single ultrasound contrast agent microbubbles using double passive cavitation detection. The Journal of the Acoustical Society of America. 2010; 127:3449–55. [PubMed: 20550244]

Kruse DE, Ferrara KW. A new imaging strategy using wideband transient response of ultrasound contrast agents. Ieee T Ultrason Ferr. 2005; 52:1320–9.

Kwan JJ, Borden MA. Microbubble dissolution in a multigas environment. Langmuir : the ACS journal of surfaces and colloids. 2010; 26:6542–8. [PubMed: 20067292]

Leighton, TG. The Acoustic Bubble. San Diego: Academic Press; 1994.

Lindsey BD, Rojas JD, Martin KH, Shelton SE, Dayton PA. Acoustic characterization of contrast-to-tissue ratio and axial resolution for dual-frequency contrast-specific acoustic angiography imaging. IEEE transactions on ultrasonics, ferroelectrics, and frequency control. 2014; 61:1668–87.

Madanshetty SI, Roy RA, Apfel RE. Acoustic microcavitation: its active and passive acoustic detection. The Journal of the Acoustical Society of America. 1991; 90:1515–26. [PubMed: 1939908]

Author Manuscript Author Manuscript Author Manuscript Author Manuscript

Martin KH, Lindsey BD, Ma J, Lee M, Li S, Foster FS, Jiang X, Dayton PA. Dual-Frequency Piezoelectric Transducers for Contrast Enhanced Ultrasound Imaging. Sensors. 2014; 14:20825–42. [PubMed: 25375755]

Nakamura Y, Yasuoka H, Tsujimoto M, Imabun S, Nakahara M, Nakao K, Nakamura M, Mori I, Kakudo K. Lymph vessel density correlates with nodal status, VEGF-C expression, and prognosis in breast cancer. Breast cancer research and treatment. 2005; 91:125–32. [PubMed: 15868440]

Porter TM, Smith DA, Holland CK. Acoustic techniques for assessing the Optison destruction threshold. Journal of ultrasound in medicine : official journal of the American Institute of Ultrasound in Medicine. 2006; 25:1519–29. [PubMed: 17121946]

Porter TR, Xie F. Transient myocardial contrast after initial exposure to diagnostic ultrasound pressures with minute doses of intravenously injected microbubbles. Demonstration and potential mechanisms. Circulation. 1995; 92:2391–5. [PubMed: 7586336]

Radhakrishnan K, Bader KB, Haworth KJ, Kopechek JA, Raymond JL, Huang SL, McPherson DD, Holland CK. Relationship between cavitation and loss of echogenicity from ultrasound contrast agents. Physics in medicine and biology. 2013; 58:6541–63. [PubMed: 24002637]

Schutt EG, Klein DH, Mattrey RM, Riess JG. Injectable microbubbles as contrast agents for diagnostic ultrasound imaging: The key role of perfluorochemicals. Angew Chem Int Edit. 2003; 42:3218–35.

Shankar PM, Dala Krishna P, Newhouse VL. Advantages of subharmonic over second harmonic backscatter for contrast-to-tissue echo enhancement. Ultrasound Med Biol. 1998; 24:395–9. [PubMed: 9587994]

Shelton SE, Lee YZ, Lee M, Foster FS, Aylward SR, Dayton PA. Quantification of microvascular tortuosity during tumor evolution utilizing acoustic angiography. Ultrasound in medicine & biology. In review.

Shi WT, Forsberg F. Ultrasonic characterization of the nonlinear properties of contrast microbubbles. Ultrasound in Medicine and Biology. 2000; 26:93–104. [PubMed: 10687797]

Shi WT, Forsberg F, Hall AL, Chiao RY, Liu JB, Miller S, Thomenius KE, Wheatley MA, Goldberg BB. Subharmonic imaging with microbubble contrast agents: initial results. Ultrasonic imaging. 1999; 21:79–94. [PubMed: 10485563]

Sijl J, Gaud E, Frinking PJ, Arditi M, de Jong N, Lohse D, Versluis M. Acoustic characterization of single ultrasound contrast agent microbubbles. The Journal of the Acoustical Society of America. 2008; 124:4091–7. [PubMed: 19206831]

Skyba DM, Price RJ, Linka AZ, Skalak TC, Kaul S. Direct in vivo visualization of intravascular destruction of microbubbles by ultrasound and its local effects on tissue. Circulation. 1998; 98:290–3. [PubMed: 9711932]

Streeter JE, Gessner R, Miles I, Dayton PA. Improving sensitivity in ultrasound molecular imaging by tailoring contrast agent size distribution: in vivo studies. Molecular imaging. 2010; 9:87–95. [PubMed: 20236606]

Takahashi Y, Kitadai Y, Bucana CD, Cleary KR, Ellis LM. Expression of vascular endothelial growth factor and its receptor, KDR, correlates with vascularity, metastasis, and proliferation of human colon cancer. Cancer Res. 1995; 55:3964–8. [PubMed: 7664263]

Talu E, Hettiarachchi K, Zhao S, Powell RL, Lee AP, Longo ML, Dayton PA. Tailoring the size distribution of ultrasound contrast agents: possible method for improving sensitivity in molecular imaging. Molecular imaging. 2007; 6:384–92. [PubMed: 18053409]

Thieme, GA.; Shung, KK. Ultrasonic scattering in biological tissues. Boca Raton, FL: CRC Press; 1992.

Thomas DH, Butler MB, Anderson T, Steel R, Pye SD, Poland M, Brock-Fisher T, McDicken WN, Sboros V. Single microbubble response using pulse sequences: initial results. Ultrasound Med Biol. 2009; 35:112–9. [PubMed: 18845380]

Tung YS, Vlachos F, Choi JJ, Deffieux T, Selert K, Konofagou EE. In vivo transcranial cavitation threshold detection during ultrasound-induced blood-brain barrier opening in mice. Physics in medicine and biology. 2010; 55:6141–55. [PubMed: 20876972]

Vignon F, Shi WT, Powers JE, Everbach EC, Liu J, Gao S, Xie F, Porter TR. Microbubble cavitation imaging. IEEE transactions on ultrasonics, ferroelectrics, and frequency control. 2013; 60:661–70.

Author Manuscript Author Manuscript Author Manuscript Author Manuscript

Vos HJ, Guidi F, Boni E, Tortoli P. Method for microbubble characterization using primary radiation force. IEEE transactions on ultrasonics, ferroelectrics, and frequency control. 2007; 54:1333–45.

Yasui K, Lee J, Tuziuti T, Towata A, Kozuka T, Iida Y. Influence of the bubble-bubble interaction on destruction of encapsulated microbubbles under ultrasound. The Journal of the Acoustical Society of America. 2009; 126:973–82. [PubMed: 19739710]

Yeh CK, Su SY. Effects of acoustic insonation parameters on ultrasound contrast agent destruction. Ultrasound Med Biol. 2008; 34:1281–91. [PubMed: 18343019]

Zhao SK, Ferrara KW, Dayton PA. Asymmetric oscillation of adherent targeted ultrasound contrast agents. Applied Physics Letters. 2005; 87

Author Manuscript Author Manuscript Author Manuscript Author Manuscript

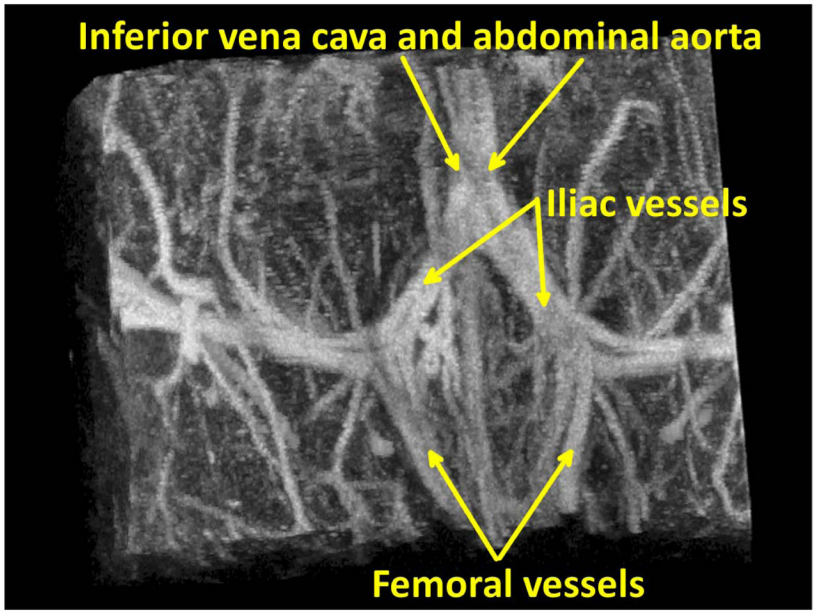


**Figure 1.**

High resolution, high-contrast images are acquired using a mechanically-steered dual frequency transducer transmitting at 4 MHz and receiving at 30 MHz in a 3-month-old C3(1)/Tag mouse. The image shows the bifurcation of the inferior vena cava and abdominal aorta into bilateral iliac vessels, as well as further bifurcation into femoral vessels.

Author Manuscript Author Manuscript Author Manuscript Author Manuscript

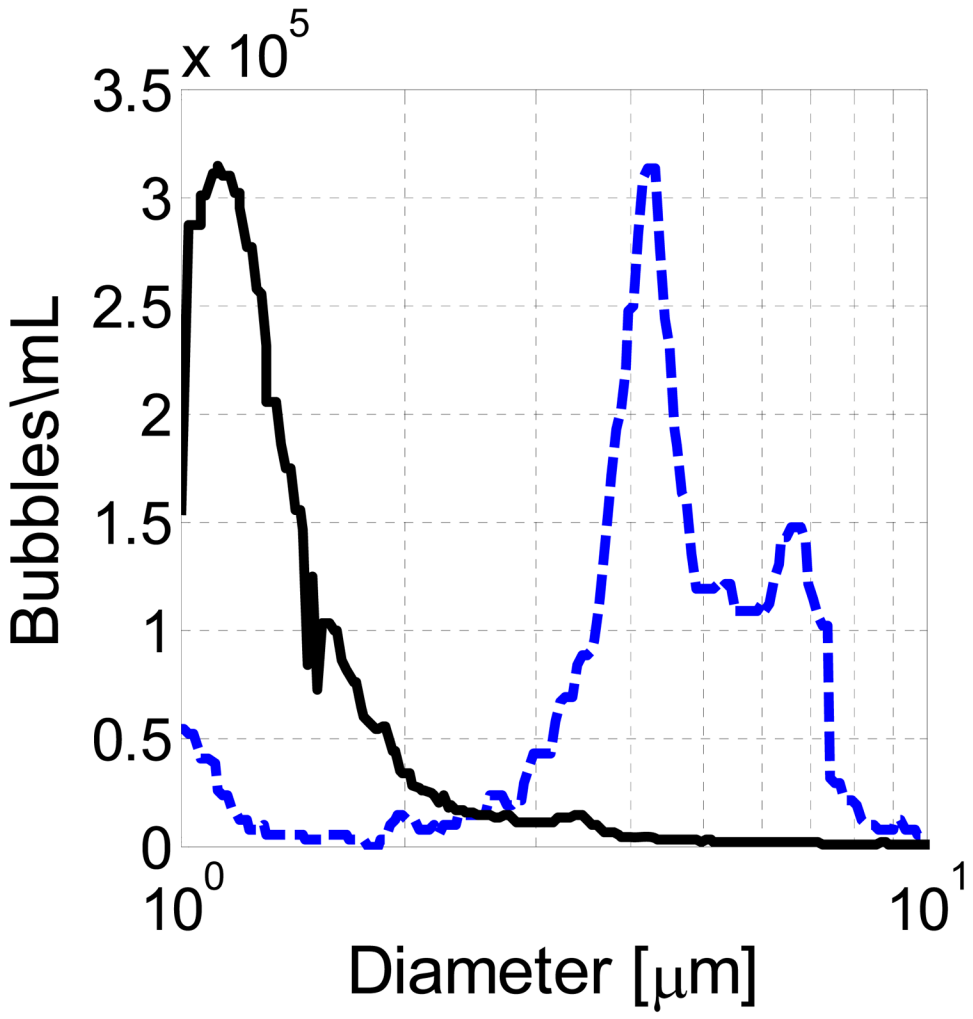


**Figure 2.**

The 4 and 1 μm microbubble populations used in this work had modes of 4.5 μm and 0.6 μm, respectively. Bubbles were diluted such that only a single microbubble was visible within the optical focus.

Author Manuscript Author Manuscript Author Manuscript Author Manuscript

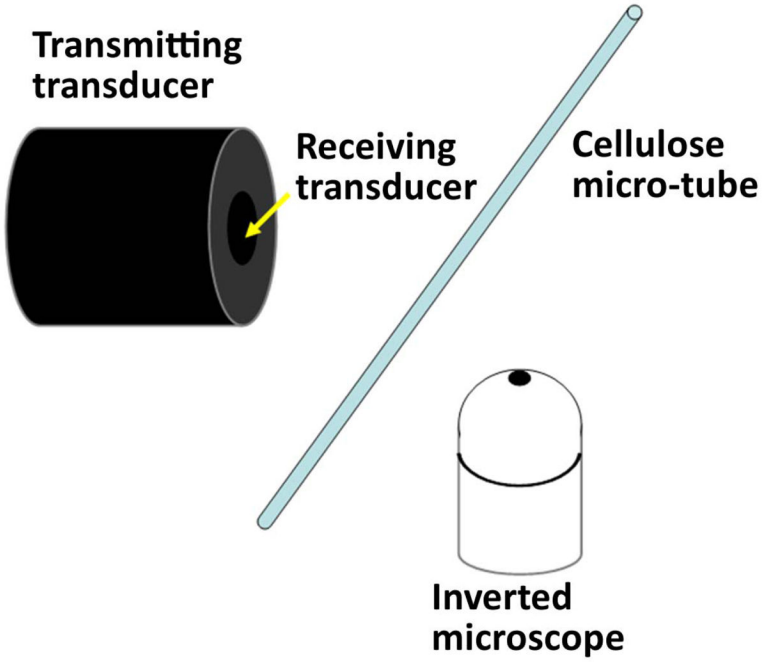


**Figure 3.**

The experimental setup used in this work consists of a 200 μm cellulose tube positioned at the common focus of a 2.25 MHz transmitting transducer, a 10 MHz receiving transducer, and an inverted microscope.

Author Manuscript Author Manuscript Author Manuscript Author Manuscript

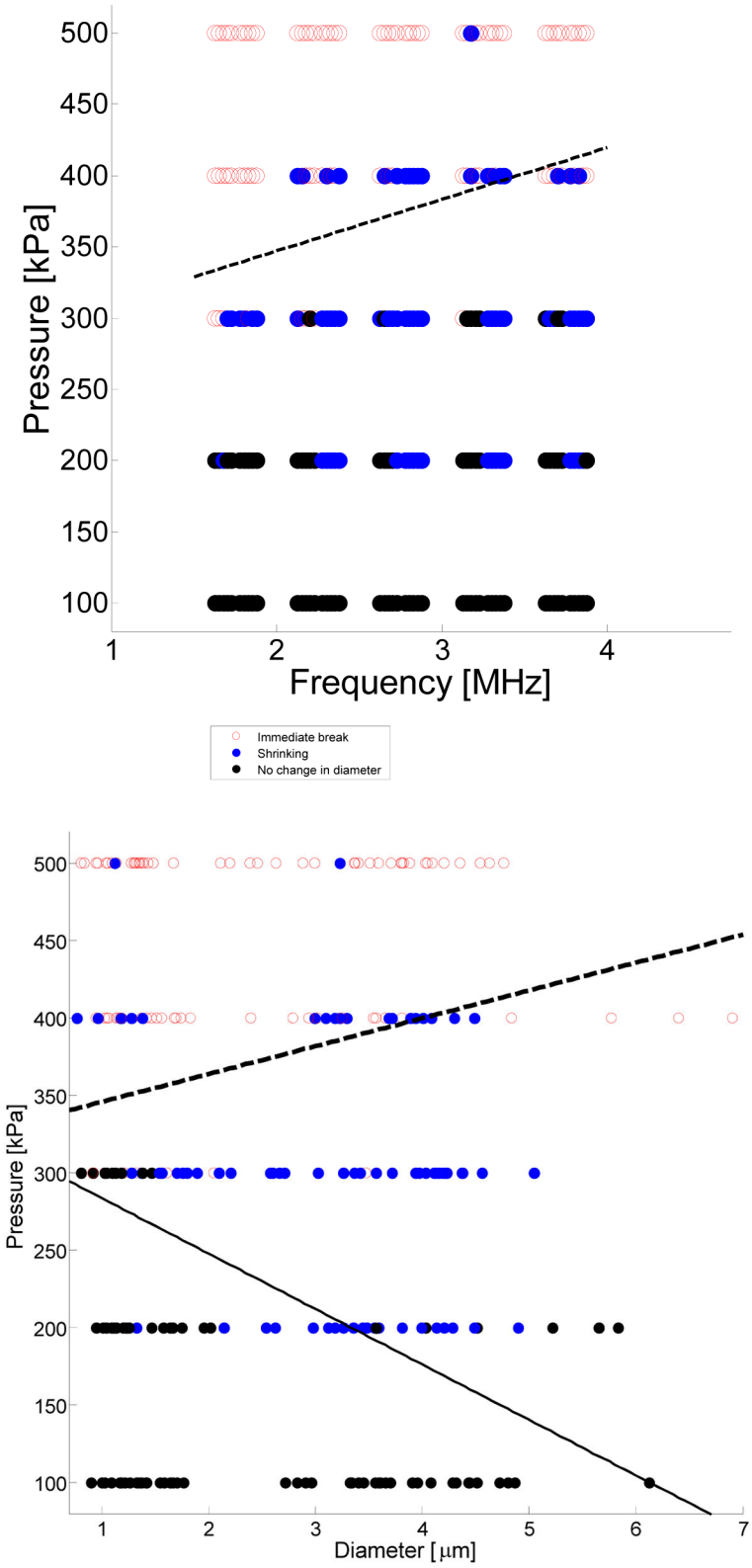


**Figure 4.**

Author Manuscript Author Manuscript Author Manuscript Author Manuscript

**Figure 4A.** Observed shell fragmentation and shrinking with varying frequency and pressure in all bubbles. At each frequency/pressure combination, the first five bubbles come from a 1 μm distribution and the last five bubbles come from a 4 μm distribution.

**Figure 4B.** Observed shell fragmentation and shrinking with varying diameter and pressure in all bubbles.

Author Manuscript Author Manuscript Author Manuscript Author Manuscript

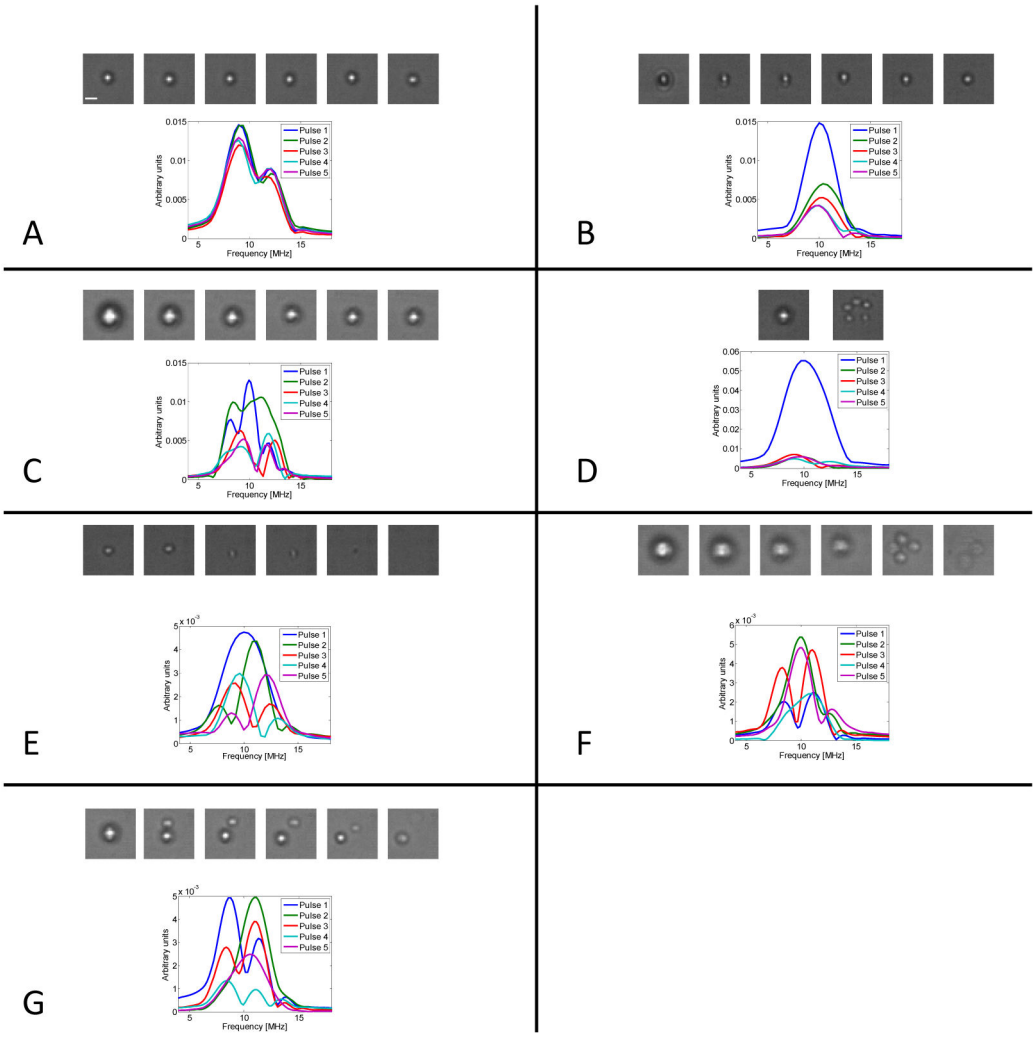


**Figure 5.**

**(A)** No change in diameter is observed in this set of recordings at 3.75 MHz, 300 kPa for a 1 μm bubble. Scale bar indicates 1 μm. **(B)** A single decrease in bubble diameter is observed in this set of recordings at 1.75 MHz, 300 kPa for a 1 μm bubble. **(C)** Multiple shrinking events are visible optically and in the corresponding acoustic signals recorded in a 4 μm bubble at 1.75 MHz, 200 kPa. **(D)** A 4 μm-diameter bubble breaks immediately upon transmission of a 1.75 MHz, 500 kPa pulse. **(E)** A 1 μm bubble shrinks several times, then disappears without visible shell fragmentation due to application of a 2.25 MHz, 300 kPa pulse. **(F)** A 4 μm bubble shrinks then breaks with visible shell fragmentation upon transmission of a 2.75 MHz, 500 kPa pulse. The large bubble breaks on the fourth pulse, while the remnant smaller bubbles break on the fifth pulse. **(G)** A 4 μm bubble breaks into twosmaller bubbles after the transmission of the first pulse at 2.25 MHz, 400 kPa. The smaller bubble breaks on the fourth pulse.

Author Manuscript Author Manuscript Author Manuscript Author Manuscript

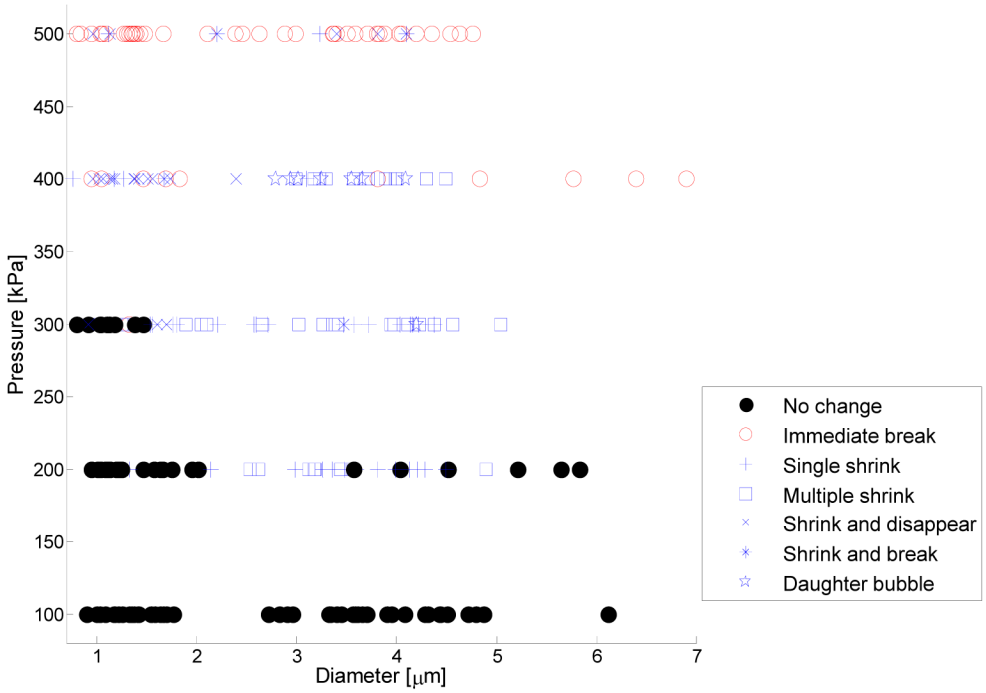


**Figure 6.**
Diameter-pressure relationship including all subcategories of shrinking bubbles.

Author Manuscript Author Manuscript Author Manuscript Author Manuscript

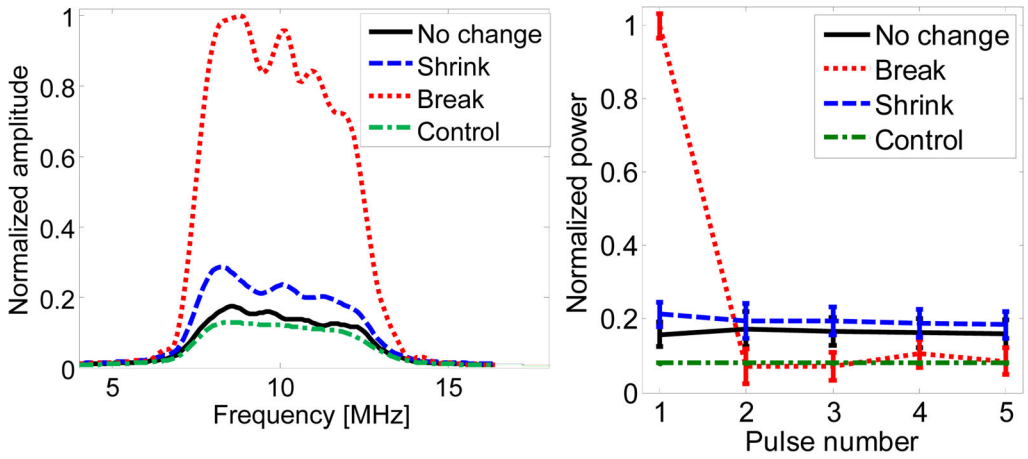


**Figure 7.**

**Figure 7A.** Mean amplitude spectra acquired after the first pulse in the absence of bubbles (green dashed-dotted line), in the presence of an unchanging, intact bubble (solid black line), a shrinking bubble (blue dashed line) and a breaking bubble (red dotted line) for 1 um (left) and 4 um (right) bubbles. All plots are normalized to the peak of the breaking bubble spectrum.

**Figure 7B.** Received power following each of five successive pulses for intact (black line), shrinking (dashed blue line) and breaking (dotted red line) bubbles. No bubble was present in the "control" case.

Author Manuscript Author Manuscript Author Manuscript Author Manuscript

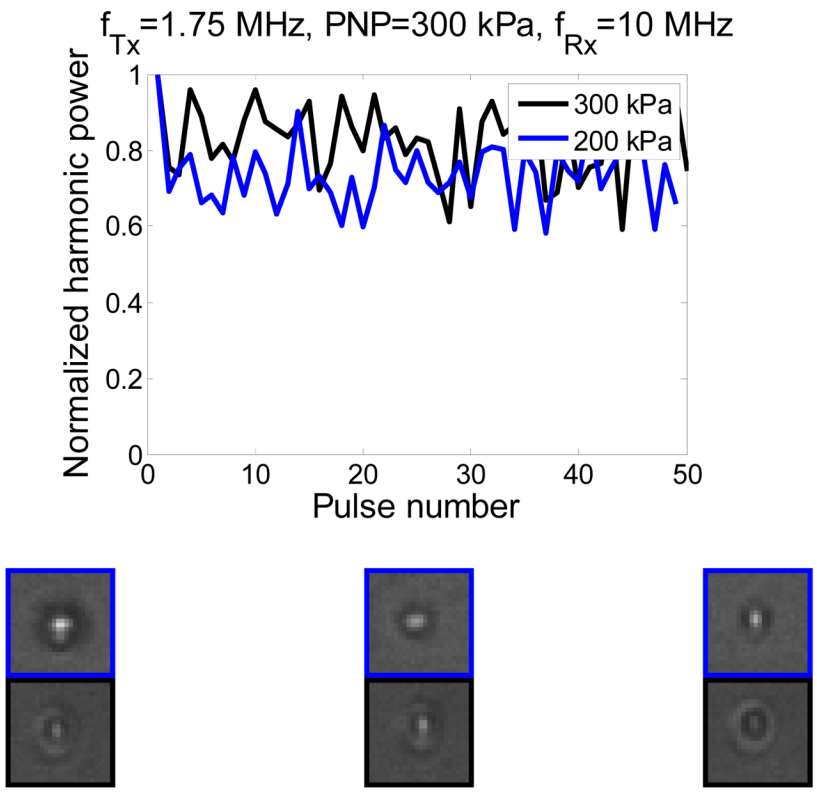


**Figure 8.**

Acoustic power and corresponding optical images of two 1 μm bubbles due to repeated transmission of 1 cycle, 1.75 MHz pulses at 200 and 300 kPa.

Author Manuscript Author Manuscript Author Manuscript Author Manuscript

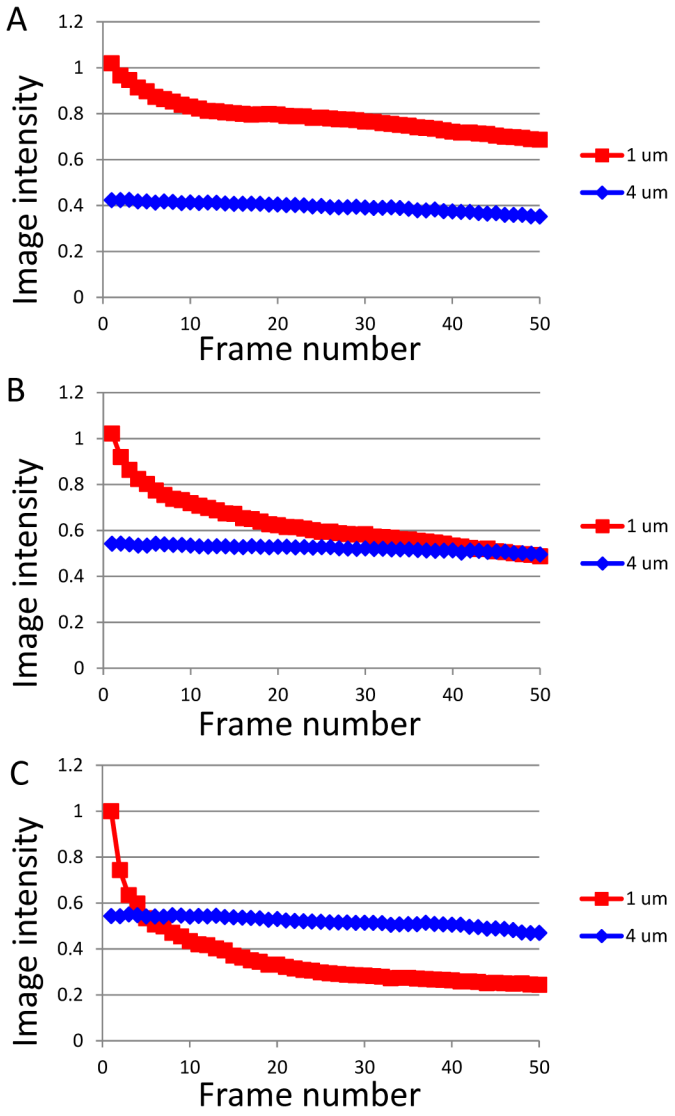


**Figure 9.**

Mean non-normalized image intensity vs. frame number for bubbles in a tube at (A) 300 kPa, (B) 350 kPa, and (C) 400 kPA.

Author Manuscript Author Manuscript Author Manuscript Author Manuscript

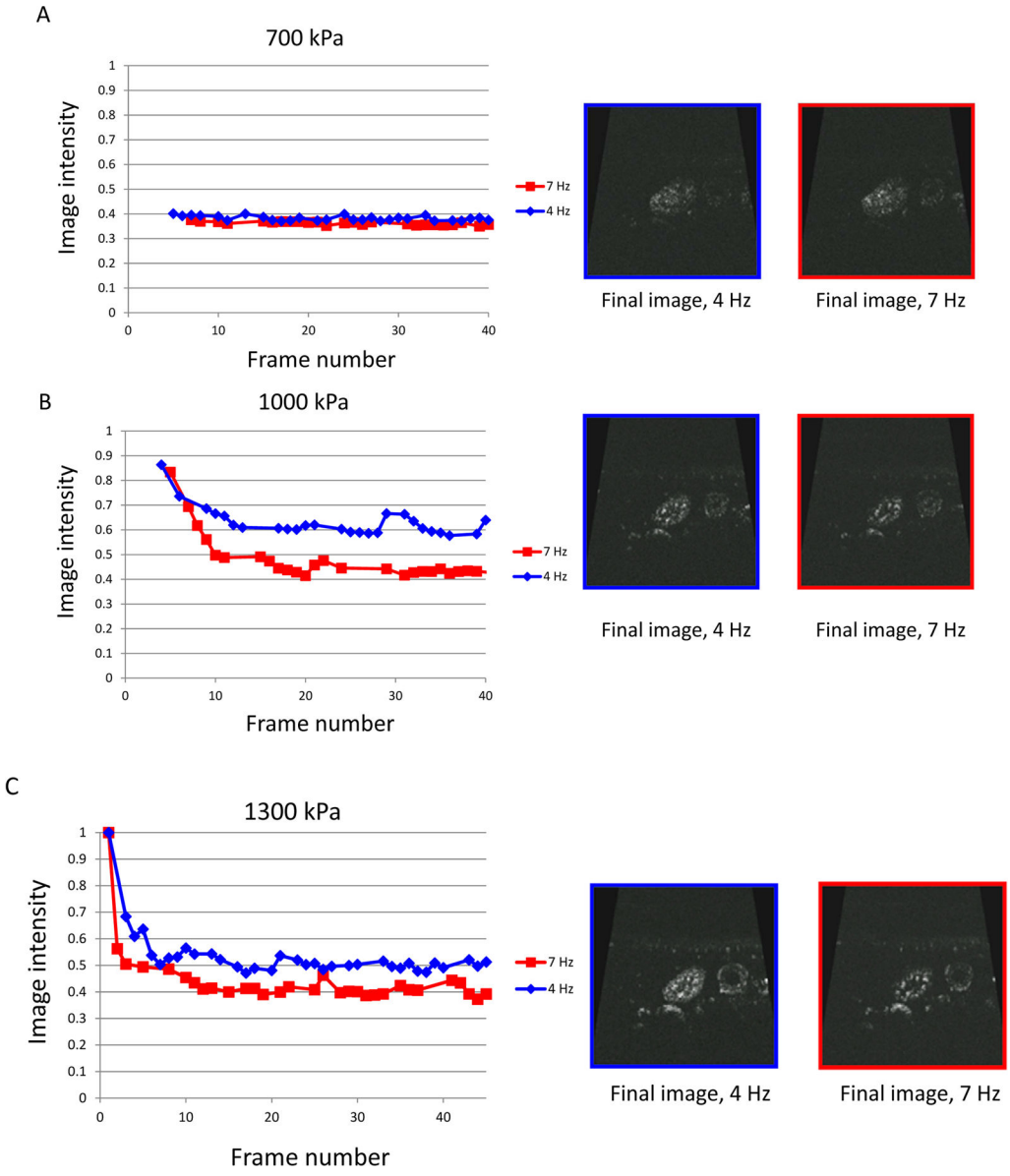


**Figure 10.**

Mean non-normalized image intensity as a function of frame (pulse) number during in vivo imaging at two frame rates. Imaging was performed at 4 MHz and (A) 700 kPa, (B) 1000 kPa, and (C) 1300 kPa using 1 μm bubbles.